Initial cathodic reactivity of intermetallic particles in 7175 aluminum alloy buried under 6 μm thick anodized oxide layer revealed by in-situ reflective microscopy

Florian Raffin, Aleksei Makogon, Frédéric Kanoufi, Jacques Echouard, Viacheslav Shkirskiy, Polina Volovitch

Electrochimica Acta 492 (2024) 144155

Contents lists available at ScienceDirect

Electrochimica Acta

journal homepage: www.journals.elsevier.com/electrochimica-acta

Initial cathodic reactivity of intermetallic particles in 7175 aluminum alloy buried under 6 μm thick anodized oxide layer revealed by *in-situ* reflective microscopy

Florian Raffin [a], Aleksei Makogon [b], Frédéric Kanoufi [b], Jacques Echouard [c], Viacheslav Shkirskiy [b,*], Polina Volovitch [a,*]

[a] Chimie ParisTech-CNRS, PSL Research University, Institut de Recherche de Chimie Paris (IRCP), 11 rue Pierre et Marie Curie, Paris 75005, France
[b] Université Paris Cité, ITODYS, CNRS, Paris 75013, France
[c] Safran Landing Systems, 7 Rue Général Valérie André, Vélizy-Villacoublay 78140, France

ARTICLE INFO

Keywords:
Silicate sealed TSA anodized aluminum alloy
Intermetallic particles
Cathodic reactivity
Buried interface
In situ reflective microscopy

ABSTRACT

An *in-situ* approach to buried metal/oxide interface is proposed, allowing to correlate an initial cathodic reactivity detected on the top surface of a several μm thick rough oxide with the distribution of intermetallic particles (IMPs) in the substrate alloy close to metal/oxide interface. A 7175 aluminum alloy with a 6 μm thick oxide layer (tartaric-sulfuric acid anodized and silicate sealed) was exposed to applied cathodic potential of – 1.4 V vs Ag/AgCl in 10 mM NaCl aqueous solution for 900 s. Sites of initial cathodic reactivity generated gas bubbles and were localized on the surface thanks to high resolution *in-situ* reflective optical microscopy and image treatment of the recorded movie. Buried metal/oxide interface was accessed and studied *ex situ* by scanning electron microscopy and electron dispersive spectroscopy. Areas with high density of bubble initiation sites on the top surface correlated with the high density of IMPs in the substrate alloy close to the buried metal/oxide interface. For more than 80% of the 145 analyzed bubble initiation sites the distance between the (X,Y) position of the generated bubble center and the (X,Y) position of the nearest buried IMP was less than the average diameter of the bubble (6 ± 2 μm).

1. Introduction

In situ monitoring of corroding surfaces characteristics could bring an important and unique insight into kinetics and mechanisms of corrosion [1,2]. Multiple electrochemical techniques such as the electrochemical impedance spectroscopy (EIS) and its local variant (LEIS), scanning vibrating electrode technique (SVET) or scanning electrochemical microscopy (SECM) allows to assess *in situ* the evolution of the electrochemical surface properties in contact with aggressive electrolytes [3–16]. Nowadays the electrochemical methods are more and more often coupled with live optical microscopy, so-called Time-Lapse Microscopy (TLM) [4,9,17]. This coupling allows to complete the electrochemical information with the data about localized evolution of the surface morphology, local pH (with help of the pH indicators) etc. Significant progress has been achieved in the application of high resolution optical microscopy to monitor reactivity mechanisms on metallic surfaces using reflective microscopy (RM) [17–21]. The principle of RM is to record *in situ* videos of the evolving surface by reflecting optical light when the objective of the microscope is immersed in the electrolyte in front of the corroding surface. Because the intensity of the reflected light is proportional to the refractive index, any surface modification can be detected and quantified by image analysis. Great advantage of RM is that it can combine a wide view field of several mm with high spatial resolution (theoretical limit for visible light is around 200 nm) and high sensitivity (as low as 30 nm size objects) [18]. So far, most applications of RM in corrosion field have been made on metallic surfaces thanks to their high reflectivity [19,21] or to monitor the evolution in artificially scratched protective coating (up to the metal) [22]. In contrast, to our knowledge these technics have never been applied to understand the evolution of metallic surface buried under a several μm thick and rough coating, like for instance that obtained by anodizing processes, largely used in corrosion protection of aluminum alloys.

Surface treatments of structural aluminum alloys are necessary to increase the corrosion resistance because of the presence of intermetallic

* Corresponding authors.
E-mail addresses: viacheslav.shkirskiy@cnrs.fr (V. Shkirskiy), polina.volovitch@chimieparistech.psl.eu (P. Volovitch).

https://doi.org/10.1016/j.electacta.2024.144155
Received 4 January 2024; Received in revised form 22 March 2024; Accepted 24 March 2024
Available online 30 March 2024

particles (IMPs). IMPs are responsible of desired mechanical properties but make the material sensitive to corrosion because of micro-galvanic coupling between them and the surrounding aluminum matrix [23, 24]. Most of these surface treatment technologies typically include several steps. During acid pickling most of the IMPs close to the surface are removed [25–27]. Anodizing is then usually performed to form a several μm – thick and non-conductive protective layer, under which the remaining IMPs are then buried. Finally, porous anodized oxide is sealed to improve barrier properties. The formed oxide layer is expected to protect the material from the effect of micro-galvanic coupling. Therefore, aqueous reactivity of the anodized materials is often considered as controlled by the properties of the oxide film, disregarding possible effects of the buried IMPs. Neglecting the effects of the buried IMPs is also due to the difficulties of their detection and measurement of their electrochemical response under thick oxide. In the present work we try for the first time to elucidate the effect of IMPs buried under a 6 μm - thick anodized oxide on cathodic reactivity of TSA anodized aluminum alloys.

The main objective of this work is to adapt *in situ* reflective microscopy to studies of initial reactivity of anodized materials and to verify if there is any link between the presence of buried IMPs and the location of initial reactivity sites of anodized materials. To achieve this, the RM measurements were made during the initial steps of the accelerated cathodic degradation of 7175 aluminum alloy, protected with an oxide layer obtained by tartaric-sulfuric acid anodizing and silicate sealing. Our previous work [28] demonstrated that application of accelerated ageing cycles alternating 30 min of cathodic polarization and EIS measurements for several hours resulted the formation of micrometric size black pits generating bubbles on the surface of this system. The bubbles formation can be attributed to cathodic water reduction which becomes important at potentials lower than – 1 V vs saturated calomel electrode (SCE) (so – 0.955 V vs Ag/AgCl) [29,30] and leads to the increase of the interface alkalinity (reaction 1). The letter could also be responsible for a local dissolution of the anodized oxide film (reaction 2) visible as pits in the oxide layer.

$$2H_2O + 2e^- \rightarrow 2OH^- + H_2\uparrow \quad (1)$$

$$AlO(OH) + OH^- + H_2O \rightarrow Al(OH)_4^- \quad (2)$$

According to Usman et al. [31], in such a cycle the evolution of the surface morphology of anodized aluminum is similar to that observed in long immersion times and the EIS response decline is also similar, so morphological evolution during cathodic polarization is expected to be representative for corrosion of anodized materials. These results indicate that for anodized aluminum not only anodic but also cathodic reactions could lead to pitting and cathodic pitting initiation is therefore worst of investigation. In our previous work [28], the density of pits formed at advanced stages of degradation on machined substrate was significantly lower than their density on the rolled substrate. Strong difference in the IMPs distribution was due to the processing of the substrate alloy (machining or rolling), which is known to strongly influence the IMPs size and distribution [32,33]. Indeed, in [28] the machined substrate demonstrated small density of IMPs of relatively big size (tens of μm) while the rolled substrate was characterized with higher IMPs density and their smaller size. This led us to a hypothesis that such a localized degradation can be related to the presence of IMPs near the alloy/oxide interface. In this hypothesis the IMPs would cause preferential current path and localized attack of the protective layer at the metal/oxide interface rather than the top surface. Such a degradation mechanism could be accepted for the anodized and sealed layers for which the alkaline stability of the sealed layer is stronger than the alkaline stability of aluminum oxide but which still could allow some diffusion of oxygen and water to the metal-oxide interface. This was the case of the silicate-based sealants studied in [28], for which the anticorrosion protection of Al alloys is well known [34–37] and alkaline stability seems to be better than the alkaline stability of alumina [38]. The proposed in [28] mechanisms however comes from the observations at advanced stage of degradation, when the pit size is very big and it was hence impossible to directly correlate the pit initiation and the presence of an intermetallic particle lose to the metal-oxide interface. It stays hence speculative until the reactivity initiation can be observed.

The current work suggests a new methodology able to verify if the initial cathodic reactivity indeed occurs at the intermetallic particles buried directly underneath the metal-oxide interface. For this, first, high-resolution RM is proposed to identify and localize, through optical images, the areas where the H_2 bubbles were nucleated at the oxide/aqueous solution interface. Second, a procedure allowing an *ex situ* analysis of the buried interface under the *in situ* analyzed area by Scanning Electron Microscopy (SEM) is proposed. Finally, a new data treatment procedure is used, which allows to correlate the RM reactivity map and the microstructure of buried interface imaged by SEM and to verify if initial cathodic reactivity sites can be associated with the buried at the alloy / oxide interface IMPs.

2. Experimental

2.1. Materials

The AA7175-T6 sheet was produced by rolling, resulting in thicknesses of 0.2 mm and cut into specimens of 10 × 12 cm^2 area. Nominal chemical composition of the alloy is given in Table 1. Anodizing and sealing were made in pilot conditions (200 L bath) on the plates previously degreased in a 10% vol. alkali-based bath (silicate-free, pH = 9) for 10 min at 45 °C. Rinsing with deionized water was applied between each step. Etching was then performed during 10 min at 50 °C in a mix of 42% vol. acid-based solution (sulfuric and nitric acid) and 10% vol. ferric sulfate-based solution (bath pH < 1). The specimen was then anodized in a tartaric/sulfuric acid (TSA) bath (80 g/L of $C_4H_4O_6$ and 40 g/L of H_2SO_4) at 37 °C for 35 min. The applied voltage was 14 V, a value reached after 5 min of voltage ramp, included in the time specified above.

A two-step sealing was performed. The first step was a pre-treatment consisting in an immersion into a commercial solution, referred as impregnation A for confidentiality purpose, based on a mix of Cr(III) and Zr(IV) salts. Impregnation A was performed at 40 °C for 10 min. The sealing step was performed at 98 °C for 20 min in an alkaline silicate-based bath, with a concentration of 20 g/L. The average thickness of the obtained anodized and sealed layers was 6.3 ± 0.5 μm, measured by an eddy current coating thickness gage.

After degradation and before SEM observation, polishing was performed with SiC disks, from P2000 grade and finally with P4000 grade until reaching the alloy which was easily controlled by a sharp change of reflectivity between the oxide and the metal.

A system of coordinates was necessary for further identification of the observed in RM zone and its correlation with the images obtained after polishing. So, before the degradation experiment, a landmark was defined by a hand-made scratch (cross-shaped) on the surface of the samples. Evidently, the areas close to the scratch were excluded from the analysis in order to avoid the effects of this damaged zone. Only the bubbles formed far from the scratch were analyzed.

2.2. Scanning electron microscope (SEM)

The surface morphology and the identification of IMPs was performed by SEM-EDX on a Gemini SEM 360 from Zeiss and an XFlash© 6–60 from Bruker. The operating voltage was 15 keV, with an aperture size of 30 μm. Secondary electron (SE) images and back scattered electron (BSE) images as well as elemental analysis and mapping were performed.

Table 1
Nominal chemical composition of the alloys studied (wt.%).

	Si	Fe	Cu	Mn	Mg	Cr	Zn	Ti	Others	Al
AA7175	0.15	0.2	1.2–2.2	0.1	2.1–2.9	0.18–0.28	5.1–6.1	0.1	0.15	Bal.

2.3. Experimental set up and degradation procedure

A CH Instruments CHI 660A potentiostat was used to accelerate the degradation of the surface by polarization. A three-electrode set-up was employed, consisting of a graphite rod (6.6 mm diameter) as counter electrode (CE), a silver/silver-chloride (Ag/AgCl) as reference electrode (RE) and the sample as working electrode (WE). A cylindrical home-made cell with an active surface of circa 50 mm^2, delimited by an O-ring, was used. Samples were immersed in 20 mL of 0.01 M NaCl, in a stagnant electrolyte. After 60 min of open circuit potential (OCP) stabilization, a 15 min polarization at – 1.4 V vs Ag/AgCl was applied. RM video was recorded during the experiment. The setup is schematically presented in Fig. 1**a**. Taking into account that the presence of the scratch, necessary to mark the coordinate system for RM, strongly affects the measured current, an additional electrochemical measurement was made in the same conditions but using the sealed anodized sample without scratch in order to measure current density evolution under cathodic polarization of an intact sealed anodized surface. Principal steps of the analysing procedures proposed in this article are displayed in Fig. 1**b**.

2.4. Reflective microscopy (RM)

RM imaging was performed with an Olympus microscope, equipped with a water immersion objective (magnification × 10 1.00-NA, Olympus LUMPlanFLN W) with a focus distance of ca. 3.5 mm and a 10–25VDC SVCam exo541MU3 CCD camera (SVS-Vistek GmbH, 4496 × 4504 pixels, 12 bit). The size of an individual pixel was 0.24 µm. A halogen white lamp, filtered in the blue at 490 nm with an interference filter (spectral bandwidth of 20 nm), was used as the light source. Each acquired image consisted of a stack of 4 snapshots, each integrated over 10 ms, taken each 5 s for the duration of the whole test.

2.5. Details of defect detection and image correlation procedure

To facilitate the detection of defect initiation, a machine-learning based procedure was developed. Python scripts as well as original optical data are available in Zenodo (https://zenodo.org/records/10722993). As described in Section 2.4., during degradation, 4 snapshots are made on a 10 ms interval, every 5 s.

In this study, a methodology for the detection and analysis of bubbles in a sequence of images was inspired by image substraction procedure previously used for pits analysis [17–21,39]. The first step involved the calculation of image-by-image differences, which yielded a series of new images that displayed the differences between consecutive frames. These difference images were normalized and subjected to Gaussian blurring in preparation for further analysis. For clarity reasons, in the rest of this section, differential and normalized images will only be referred as "differential images".

Next, the edges of objects in the images were detected using the Canny edge-detection algorithm. Due to a high level of noise in the images, a large number of objects were initially detected. The centers of mass of these objects were then determined, and the parameters of the Canny algorithm were adjusted so that each bubble and similar objects were described by several contours. Density-based clustering using the DBScan algorithm was then applied to group the centers of mass and identify bubbles. However, some false positives were still present in the data, and manual differentiation was necessary. This was achieved by analyzing the regions where bubbles were suspected to be present in dynamics, i.e., the two frames before and after the given frame.

The scanning electron microscope (SEM) image was aligned with the optical image using affine transformations. The center of each bubble was marked on the transformed SEM image, and the nearest IMP was identified.

As the proposed methodology is quite recent and can be optimized, future iterations could benefit from the integration of neural network methods to facilitate the bubble recognition process. Thus, the detection of defect could be less time-consuming and could help reduce the number of detected false positives.

To illustrate what was counted as a bubble detection or what was a false positive, 3 different phenomena detected from the analysis are displayed in Fig. 2. Each panel consists of 5 differential images taken successively at 5 s interval during the degradation experiment. Images a), b), e) and k) to o) display only random variation in intensity (± 0.5%), which is considered as the detection limit for such samples. This means that only noise is detected. On snapshots f) to j), zones with stronger variation in intensity (± 2%) are visible. The circular shape delimiting these zones of strong intensity variation allows us to identify these areas as bubbles. However, the position of these bubbles evolves along the snapshots, meaning that the bubble was generated from another defect site which is out of the observed area and just moves through the observed area. Considering the evolution from snapshot b) to c), it is clear that a bubble is first formed on c). One can note that d) is a "negative image" of c) (because of the differential treatment), and that e) does not present anything but noise. It can be therefore concluded that the bubble is generated from b) to c) and disappeared from c) to d).

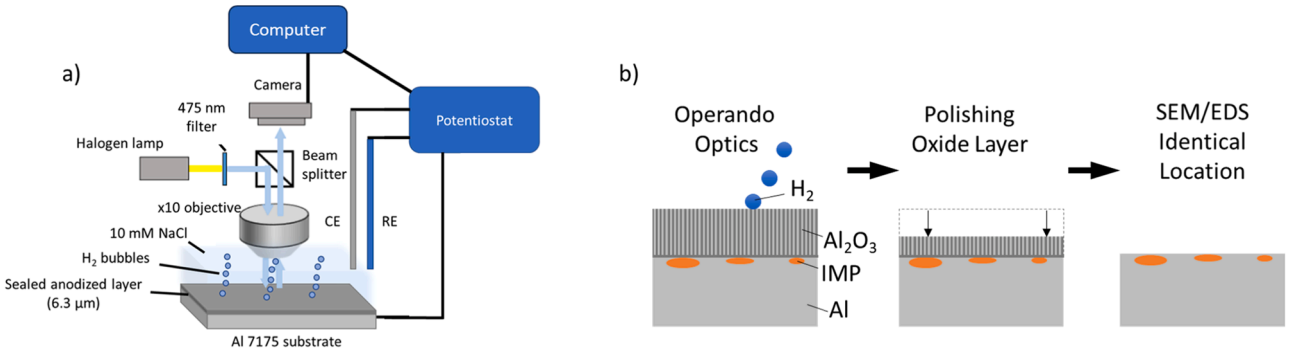

Fig. 1. Schemes (not to scale) of (a) experimental setup for an operando reflective microscopy used to localize electrochemical reactivity sites. (b) Main steps of the whole analysis process.

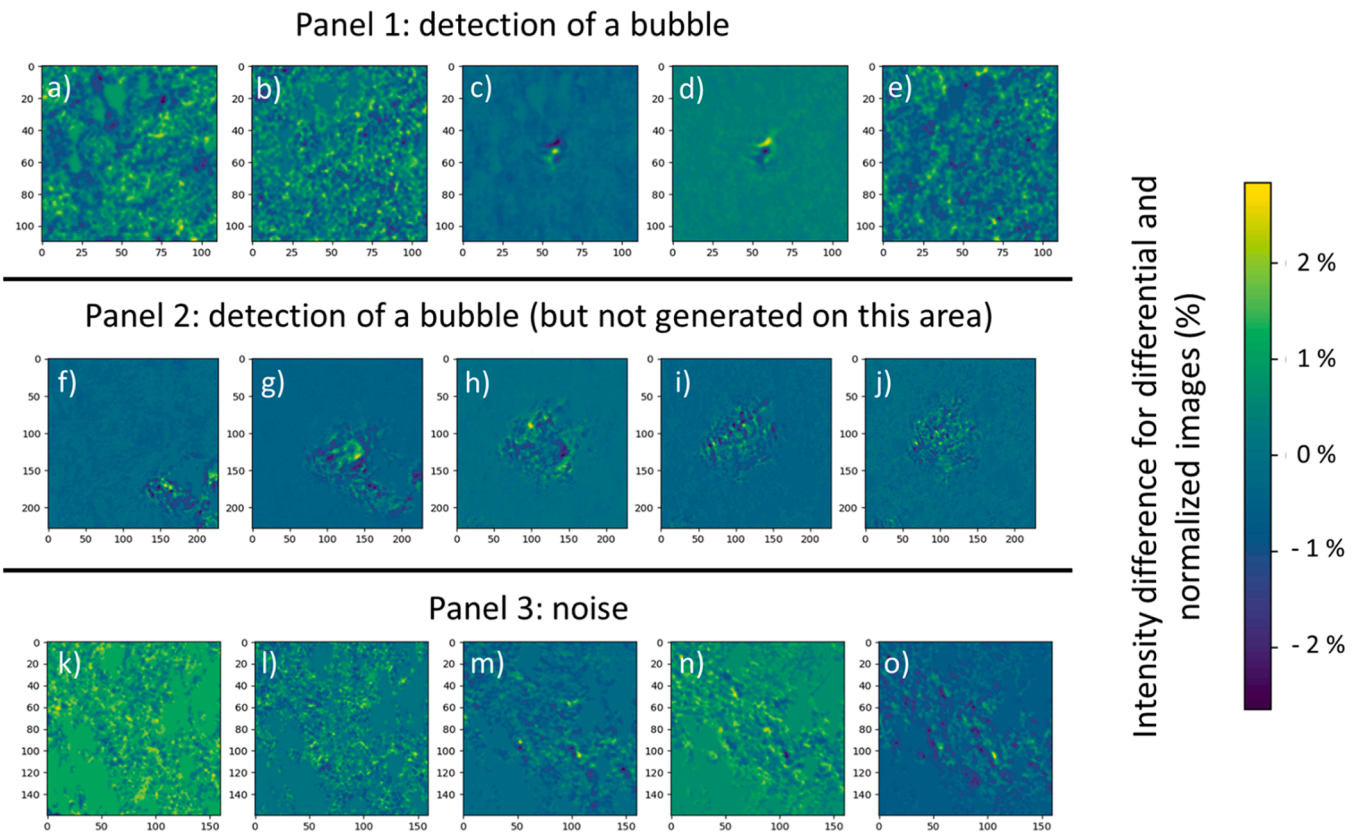

Fig. 2. Illustration of three different phenomena detected from the analysis. Each panel consists of 5 differential images taken successively at a 5 s interval during degradation. See text for more details. Scale is in pixels, where 100 pixels = 24 μm.

These 3 panels summarize well the time-consuming difficulties encountered to manually select the observed bubbles.

To estimate the bubble size was a critical step and to illustrate the errors possible in this evaluation, two diameters were measured for each of them: a minimum radius and a maximum radius. It is illustrated in Fig. 3, which displays the biggest bubbles detected during the experiment (around 14 μm diameter for the minimum radius). From the results, the highest difference between two radii was 2.4 μm, yielding $a \pm 1.2$ μm error estimation for the determination of the bubble radius (or ± 14% relative error). Regarding the optical detection limit for a detectable bubble size, previous publications demonstrated the capacity of the technics to detect bubbles with a diameter as small as 50 nm on a flat indium tin oxide (ITO) surface [40]. Compared to [40], in the current work the resolution of the optical images was lower (a pixel size of 0.24 μm), roughness of the anodized surface was higher and the optical image acquisition rate slower. As a result, the detection was possible for bubbles with a minimal diameter in order of tenths of microns. Nonetheless, these factors did not hinder our ability to derive valuable insights into the onset of localized corrosion.

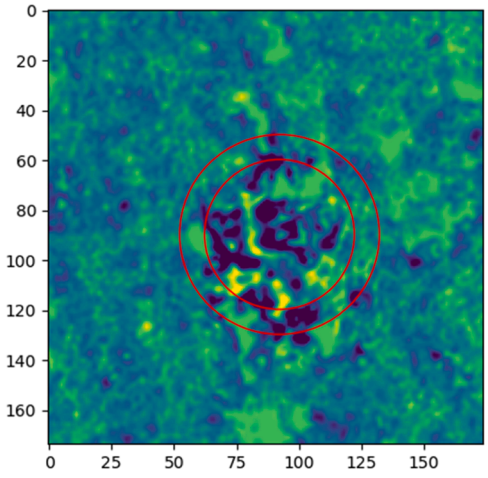

Fig. 3. Measurement of a bubble size with detection of a maximum and a minimum diameter. Scale is in pixel (1 pixel = 0.24 μm). In this case, the estimated bubble radius is 8.4 ± 1.2 μm.

3. Results and discussion

3.1. Initial state of the alloy and the oxide surfaces

To characterize the distribution and composition of intermetallic particles (IMPs) which can be found in the bulk of the substrate AA7175 alloy, the sample was polished to remove the protective oxide layer. Resulting SEM-EDS maps are illustrated in Fig. 4. Noteworthy, the SEM analysis presents only the IMPs at the surface of the alloy and does not provide a 3D concentration in the bulk of the alloy. The linear dimension of the visible IMPs is of several microns but can vary from several hundred of nm up to around ten μm. IMPs of different nature are present, some based on Si and some based on Cu/Fe. This is coherent with the literature as the main IMPs found in 7xxx series alloys are: Mg_2Si, $MgZn_2$, Al_7Cu_2Fe, Al_2Cu, Al_2CuMg and Al_3Fe among others [41,42]. Mg is detected at the same spots as Si, most likely in a form of Mg_2Si. On the other hand, Si and O also match on several particles, indicating oxidized silicon. The origin of the oxidized silicon is still unclear as it may come from the SiC polishing disks or from oxidation of Mg_2Si during the substrate polishing step [43]. While being mostly linked with Cu, indicating probably presence of Al_7Cu_2Fe, the Fe is also observed in some oxidized particles, which could be formed by selective dissolution of Al

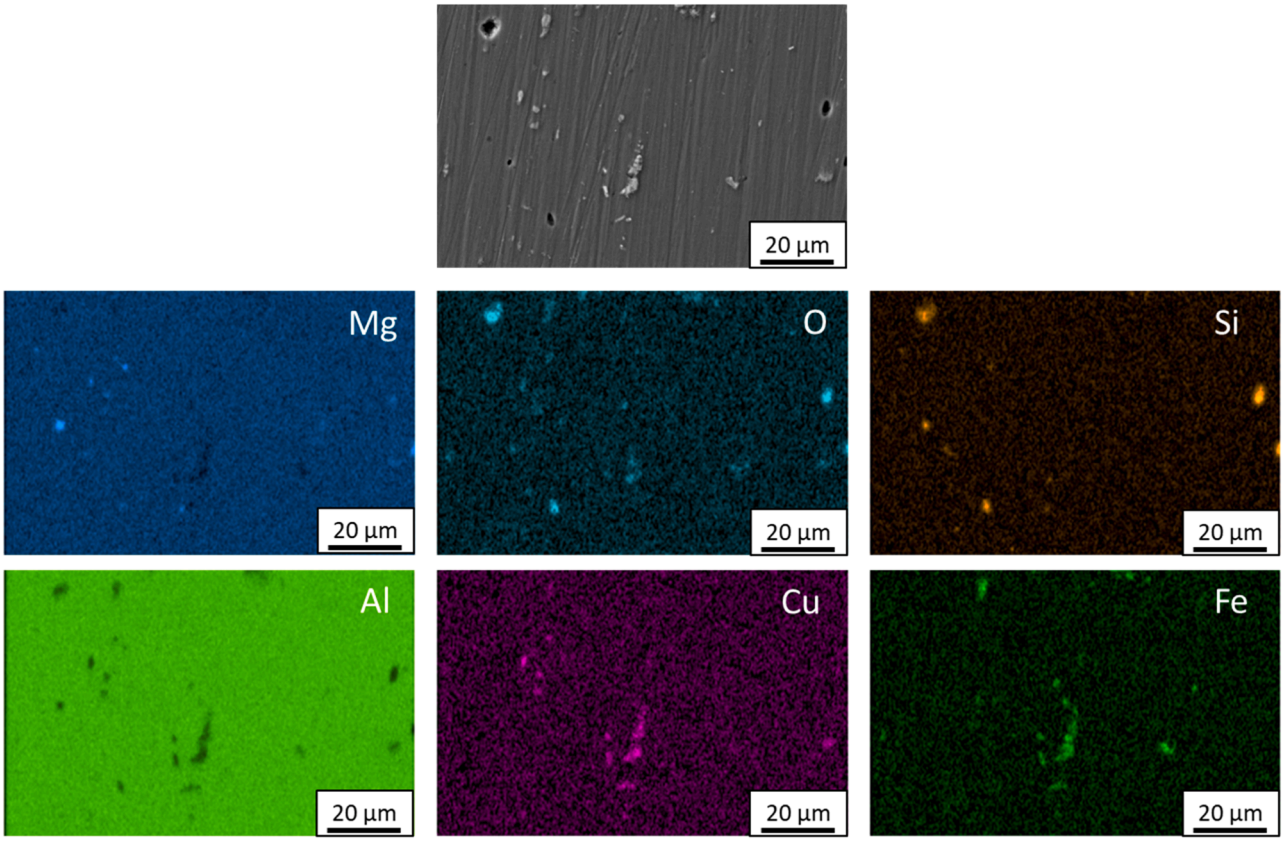

Fig. 4. SEM-EDS map of the polished 7175 before degradation.

from Al_3Fe during the polishing step.

Sealed and anodized surface appearance, before application of the accelerated ageing by polarization, was observed by reflective microscopy (RM) and scanning electron microscopy (SEM). Results are displayed in Fig. 5. With the optical microscopy, difference in the light intensity can be observed, revealing the roughness of the surface. The surface heterogeneities are visible on a micrometric scale and are spread quite homogeneously on the surface. This roughness is even more pronounced when the sample is observed by SEM. On the anodized surface, this type of micrometric cavities could be expected from such a high-mechanical strength alloy because of the preferential detachment of copper-rich intermetallic particles during the anodizing procedures [44–47]. Therefore, it is not possible to have a perfectly flat surface of the sealed oxide, as the underneath anodized layer already presents heterogeneities. In principle, these surface defects may act as preferential path for penetration of aggressive species (Cl^- for example). Some cracks are also visible on SEM images but are not present in optical images. The formation of cracks in anodized and sealed layer under SEM observation was previously reported in the literature and attributed to water desorption from the layer during the vacuum atmosphere imposed by the SEM observation [48].

3.2. *Principle of correlation search between positions of reactive sites and buried intermetallic particles*

The measurement reposes on the movie recorded by the RM of the

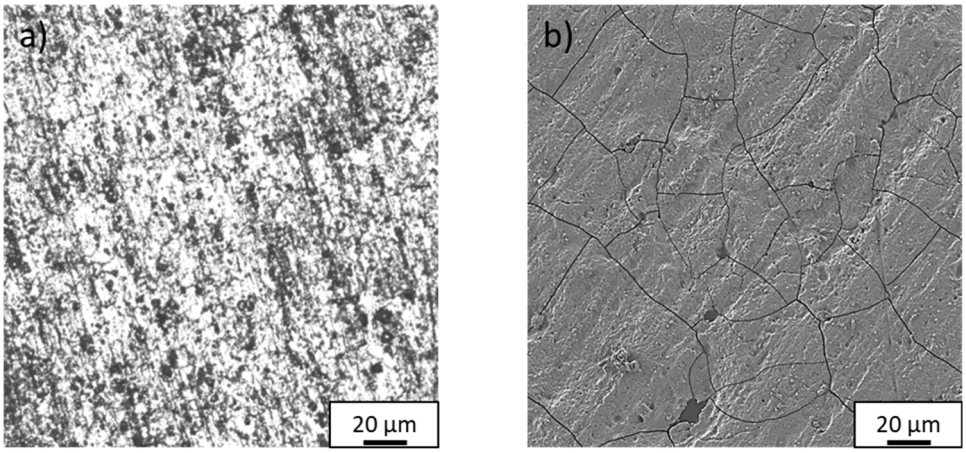

Fig. 5. Surface of the sealed and anodized sample before application of the accelerated ageing by polarization, observed by (a) reflective microscopy and (b) SEM (secondary electrons).

surface evolution under cathodic polarization. The movie is used to identify H_2 bubbles formation sites, formed by the reaction described by Eq. (1), using the image treatment procedures, described in Section 2.5. The degraded sample is then polished up to the oxide/substrate interface to reveal the buried IMPs by SEM observation. An overlay of the RM image and SEM image is made to correlate the position of the bubble initiation sites and the position of the buried IMPs. Fig. 6 summarizes the whole process used to identify the defect formation during the degradation and correlate it with the SEM image of the buried interface.

In practice, first the RM video recorded under polarization was analyzed in order to select the zones, far from the scratch, at which H_2 bubbles appeared for the first time. The first step, represented in Fig. 6**a**, already represents an example of such an area of the surface visible by the RM under cathodic polarization. To the human eye, spotting the bubble formation and visualizing any surface change can be tricky. If the bubbles formed in the scratch were very big, the bubbles formed in the intact zones were very tiny. Thus, to detect them a differential image treatment procedure described in Section 2.5. The formation of a small bubble with a short lifetime can be revealed by the differential image as illustrated in Fig. 6**b**. Thanks to the initially defined coordinate systems, the RM reactivity image can be compared with the SEM image of the underlying matrix exactly at the same area, revealed after polishing, as displayed in Fig. 6**c** and 6**d**. On the example shown in the Fig. 6, IMPs (with a linear size ranging from around 5 to 8 μm) are clearly visible on the polished surface after the oxide layer was removed. Moreover, one of them is located extremely close to the same spot where the bubbles were detected *in situ*. Such a correlation illustrates that at least in some cases the buried IMPs can act as preferential site for cathodic reactivity. Next sections present more results, which is necessary to get reliable results and for the deeper insight in the link between the buried alloy microstructure and cathodic reactivity.

3.3. *In situ reactivity and reactivity sites description*

The ageing process being operated under cathodic polarization, it is possible to reach complementary information about the sample reactivity through the macroscale electrochemical current recorded by the potentiostat. The current evolution under constant polarization is shown in Fig. 7. As discussed in the experimental section, the cathodic reactivity in the scratch was by far more intense than the reactivity of the unscratched surface (see also *in situ* RM image in supplementary information (SI), in Fig. A2). For this reason, the current shown by red cross curve in the figure was recorded in an electrochemical measurement

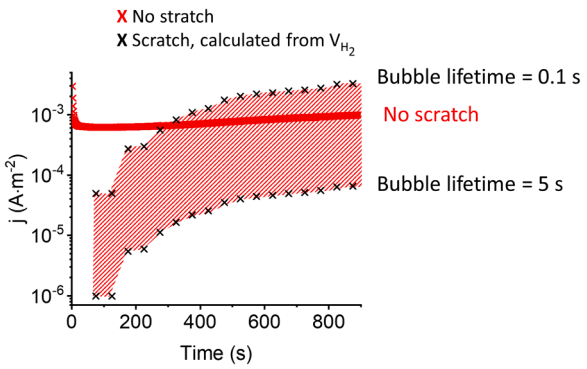

Fig. 7. Current density vs time of polarization ($E_{polarization}$ = −1.4 V vs Ag/AgCl).
X = measured electrochemical current density on an unscratched surface.
X = limits of H_2 production current density, calculated from V_{H2} and measured by RM, in assumption of different bubble lifetime, as indicated.

completed in the same electrochemical condition but using the sealed anodized sample without scratch. Additional black cross curves represent the current calculated from the volume generated by the H_2 bubbles in the experiment with the scratched surface, assuming different bubbles lifetime as indicated. The details of the calculation and a comparative analysis of these curves are given in discussion section (Section 3.5).

The aligned wide view optical and SEM images of the reacted and then polished sample are displayed in Fig. 8**a** and 8**b** respectively. As mentioned in the experimental section, the area close to scratches and between the two branches of the scratch (necessary to mark the coordinate system for RM)was not analyzed because of large bubble generation from the scratch, which darkened the area, thus making difficult identification of the bubbles arising from intact zones. Outside of this area A total of 145 bubble generation sources were detected on the surface, which are schematically represented by red dots in Fig. 8**b**. One could note that some of them are not distinguishable at this scale because they are close to each other. It can be seen from the figure, that the bubble sources are not distributed homogeneously on the surface, some zones presenting aggregates of bubble sources while other areas depleted of initiation sites. The average diameter of the detected bubbles was calculated from the methodology described in the 2.5. section and was 6 ± 0.2 μm.

To characterize the H_2 bubbles, the objects representing bubbles

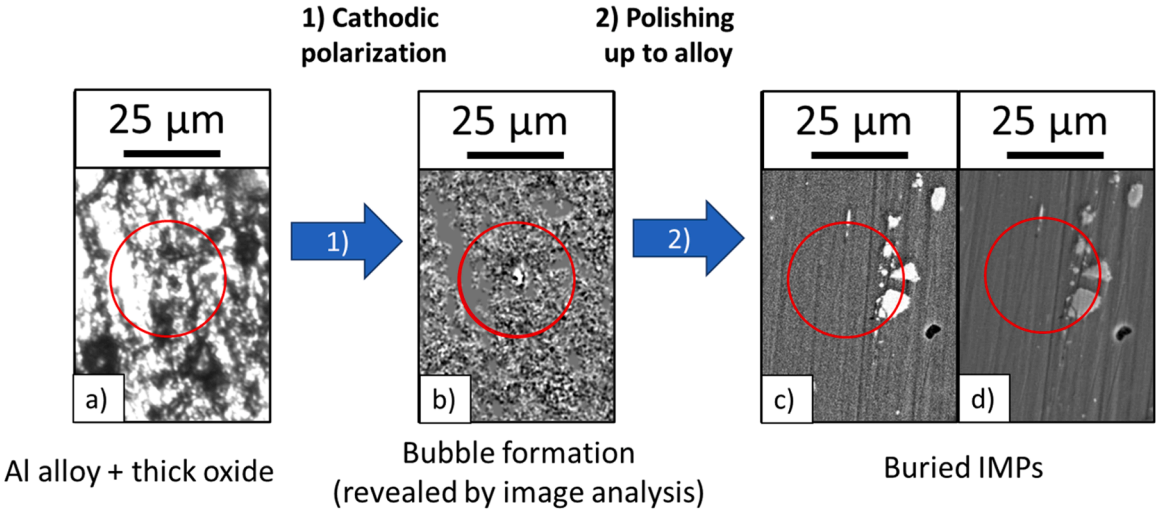

Fig. 6. Surface of the sample a) RM during cathodic polarization, b) the same RM image treated by image analysis, c) and d) respectively SEM (backscattered electrons) and SEM (secondary electrons) of the Al matrix below the protective layer. All images are at the same location. The red circle is just here to define the region of interest but does not correlate with bubble size.

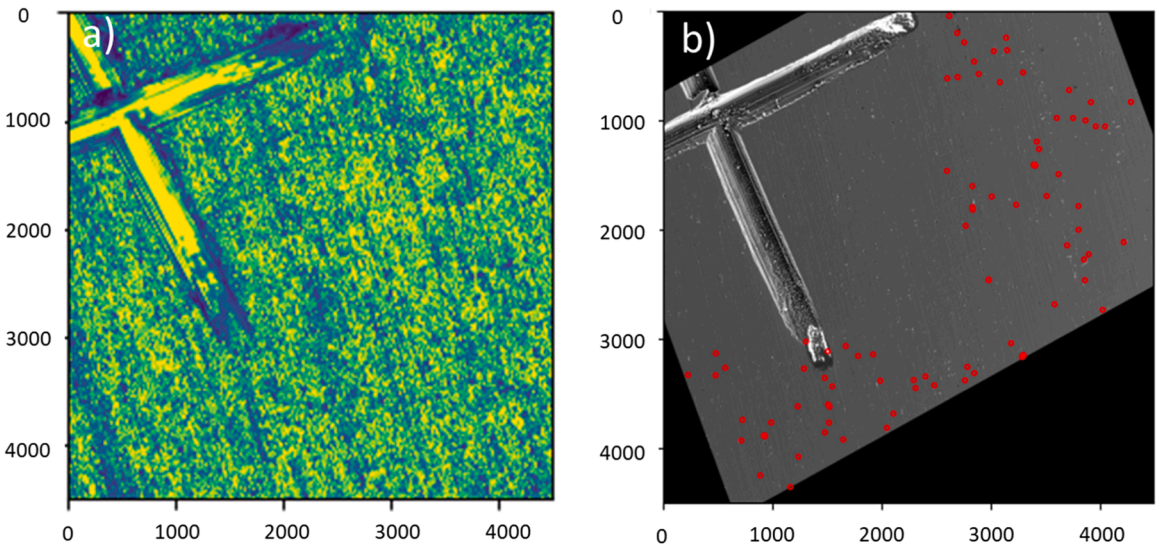

Fig. 8. (a) Optical and (b) SEM images aligned. Red dots indicate identified bubbles position. Scale is in pixels, 100 pixels = 24 μm.

detected by image analysis procedure described in Section 2.5, were analyzed. First, the number of newly formed sites of bubble evolution versus the degradation time was plotted. The result is displayed in Fig. 9**a**. It can be seen from the figure, that after 75 s of polarization, only 4 bubbles are detected. This could be related to the solubility of hydrogen. Although the number of newly formed bubbles at the end of the polarization (800 – 900 s) is higher than at the start (0 – 200 s), no clear relationship can be seen between the experiment time and number of newly formed bubbles. The volume of each individual bubble can be estimated from its measured by image analysis diameter assuming spherical bubbles shape. At each moment a cumulated volume of the evolved hydrogen can be estimated considering 5 s life time of the bubble on the surface (which means that the bubbles are formed only at the moment of the measurement on each active bubble formation site). Fig. 9**b** represents the calculated in such an approximation cumulated volume of evolved hydrogen. One should mention a linear growth of the cumulated volume with polarization time. The estimation of the evolved hydrogen will be more in detail analyzed in discussion section.

Fig. 9**c** shows the distribution of the bubbles diameters. The average bubble size (diameter) is 6 ± 0.2 μm. Considering the previously discussed error in the diameter measurement, the bubbles average size is then at most up to around 8 μm.

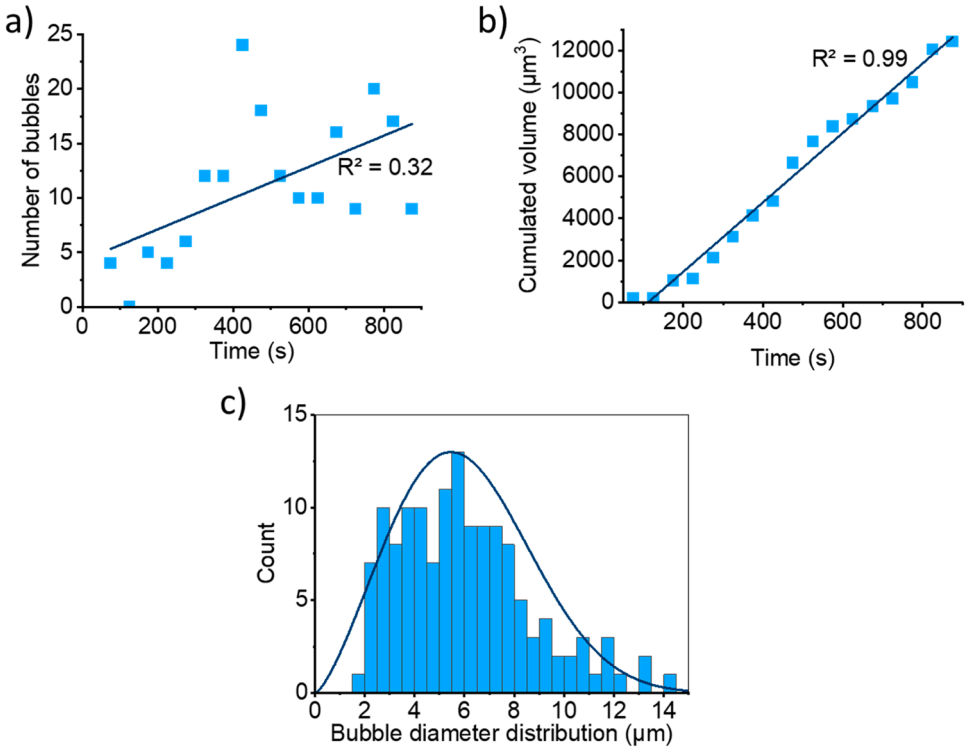

Fig. 9. H_2 bubbles characteristics.
(a) number of bubbles detected during degradation versus time
(b) cumulated volume of bubbles versus time
(c) distribution of the bubble diameters.

To verify a presumable correlation between the presence of buried IMPs and the site of bubble generation on the top surface of the oxide, the in plain distance from the projection of the center of each of 145 considered bubbles and the center of the nearest IMPs was calculated. The calculated average distance from the center of bubbles to the nearest particles was 5.7 ± 3.1 μm. The distribution of this distance for 145 bubble generation centers is given in Fig. 10**a**, showing also a Weibull fit of this distribution. It can be seen that for more than 80% of the bubbles their centers are located at a distance less than 8 μm from an intermetallic particle (59% < 6 μm and 20% < 3 μm). This means that most of the time, the bubble initiation sites are detected at a relatively close proximity of IMPs, within a range of one bubble size.

This can be observed as well on the SEM images shown in Fig. 11, which illustrates at higher resolution the overlay between the (X,Y) positions of bubble generation centers and the SEM images the buried alloy (obtained after degradation and polishing of the anodized layer up to the alloy interface). The position of bubble nucleation sites obtained from the RM videos are indicated as red circles. It should be noticed that the red circle size is not representative of the bubble size, its size is slightly higher for reading commodity. The distribution of the IMPs on these images is very heterogeneous, areas where clusters of IMPs are presents but also some IMPs depleted zones can be easily distinguished in the figure. From the position of bubbles and of the IMPs, it can clearly be seen that most of the bubbles are found in the areas where IMPs are clustered while areas depleted of IMPs have almost no bubbles.

However, it is clear from the distribution shown in Fig. 10**b** that a non-negligible amount of bubbles is formed at distances larger than one bubble radius from the buried IMPs, meaning that there is no IMP buried right below the bubble. Several hypotheses can be proposed to explain the fact that the buried IMPs are not located exactly below the bubble. First, hydrogen gas can leave the metal/oxide interface by several connected pores and generate bubbles on the roughest positions of the surface because of modification of wetting characteristics in these areas. Moreover, the columnar structure of the porous oxide is very irregular in the case of high-strength aluminum alloy because of the preferential dissolution of copper-rich IMPs during the anodizing [44–47]. This is illustrated in Fig. 12 which represents the SEM cross-section of the interface between the oxide (above the dashed red line) and the aluminum alloy (below the dashed red line). From this cross-section, it can be seen that the oxide part displays a rough sub-micrometric microstructure, attributed to the irregular porous columnar structure of the oxide formed during anodizing. On the other hand, the substrate microstructure is more homogeneous, with a quite smooth aspect. It is evident that the interface position can vary as high as around 1 μm. The porosity is therefore not strictly vertical and the path taken by the H_2 gas to reach the surface could be not linear. The later also can explain some drift between the IMPs and bubble detection coordinates.

This result also means that the roughness of the surface can be an important factor for monitoring the buried IMPs distribution in anodized samples.

Additional hypothesis can be that some IMPs, initially close to the bubble initiation site, were removed during the polishing procedure.

3.4. IMPs detected at metal/oxide interface after degradation

Once statistical analysis revealed that major part of detected bubbles is generated in vicinity of intermetallic particles, the IMPs On the buried interface were analyzed.

Fig. 13 displays an example of the surface revealed by the polishing up to the interface after degradation. Some residuals of the anodized layer are still present because of the initial roughness of this interface, as illustrated by aluminum oxide zones containing sulfur (black deposits on the surface). IMPs based on Al-Cu-Mg and Al-Cu-Fe elements are also visible (white zones). Geometrical differences can be noted between Fe containing and not containing particles. Most of the Al-Cu-Fe based particles are square-shaped (or at least have geometry characterized by sharp angles) while most part of the AlCuMg based particles are round-shaped. At the opposite of the microstructure of the bulk alloy, where some Mg_2Si was detected, only oxidized Si particles were detected after degradation. This could mean that the Mg may be selectively dissolved during anodizing, leaving then oxidized Si particles remarkable by their black round shape. Selective dissolution of Mg can be also expected during corrosion from both Mg_2Si and Al_2CuMg phases [43,49].

From the analysis of the bubbles we did not find a clear correlation between the nature of IMPs and the frequency of bubble generation sites, therefore it is highly probable that all of them could react as local cathodes. This seems to be coherent with the fact that most intermetallics (Al_2Cu, AlCuFe, Al_3Fe, etc.) are cathodic versus aluminum matrix [41]. Moreover, the alloy close to the metal/oxide interface seems to be depleted in Mg-rich IMPs, the only IMPs which are expected to be anodic versus the matrix. Besides, even these IMPs are expected to become cathodic with advancement of corrosion because of selective dissolution of Mg [49].

3.5. Discussion: reliability of observed correlation

The RM analysis of the initial cathodic reactivity on TSA anodized 7175 aluminum alloy seems to reveal that most of the hydrogen bubbles generated on the surface originates from the areas with buried intermetallic particles. One could however wonder if the studied process is representative for the reactivity of the surface or some other cathodic processes that are not visually detected could be missed. To verify, if the discussed phenomena of cathodic activation by IMPs can be considered as one of the major cathodic processes on the anodized surface, the orders of magnitude of cathodic currents measured on intact surface and calculated from the roughly estimated volume of the H_2 bubbles evolved

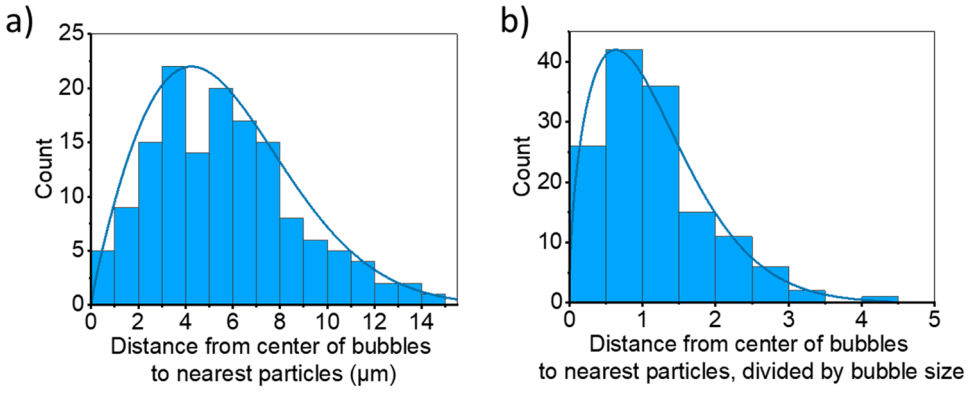

Fig. 10. a) distance from center of bubbles to the nearest particles
b) distance from center of bubbles to the nearest particles, divided by bubble size.

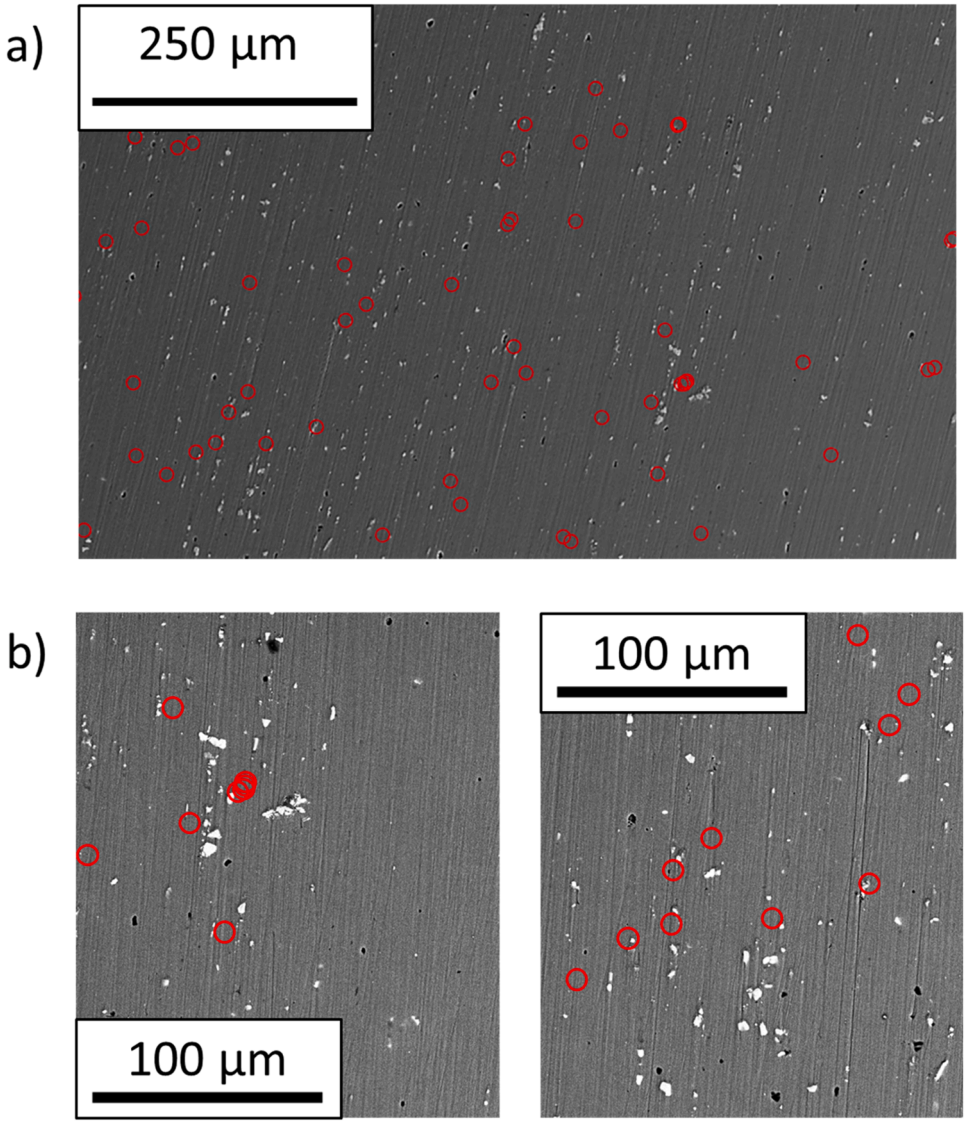

Fig. 11. Overlay of bubble initiation sites (red circles) and IMPs on the surface after degradation and polishing. (a) SE and (b) BSE. Red circle size is slightly higher than bubble size for reading commodity.

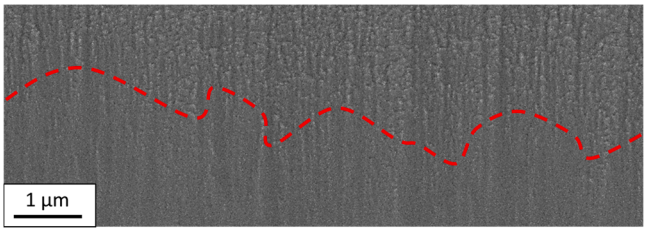

Fig. 12. SEM cross-section (SE) made by ionic polishing of the oxide-alloy interface. The interface is delimited by the dashed red line. Above this line is the porous oxide layer and below is the aluminum alloy.

in small bubbles on intact surface can be compared (Fig. 7).

The current density generated by the H_2 bubbles during the polarization was calculated from the recorded number of new bubble generation centers as a function of the electrolysis time (represented in Fig. 9**a**), the volume of each individual bubble, V, and the suggested lifetime of the gas bubble attached to the surface, here t_{H2}. Thanks to the Faraday law of electrolysis (2) the equivalent current for the formation of an individual bubble, i_B, is given by:

$$Q = i_B \times t_{H_2} = n \times F \times z \quad (2)$$

$$n = \frac{\rho \times V}{M} \quad (3)$$

where Q is the charge associated to the growth of an individual bubble, expressed in Coulomb, n is the mole number of H_2 gas generated per bubble, F is the Faraday constant (96,500 $C.m^{-1}$), z is the number of electrons ($z = 2$), M is the molar mass, ρ is the density of H_2 gas. From our experimental set-up, the lifetime of bubble is estimated at most 5 s (because snapshots were taken every 5 s and bubbles does not last more than one image) and it is expected to be at least 0.1 s, according to the literature [50], so $0.1\ s < t_{H2} < 5$ s.

Combining 2 and 3

$$i_B = \frac{\rho \times V}{M \times t_{H_2}} \times F \times z \quad (4)$$

Taking this into account, the equivalent current i_{tot} which is necessary to produce all the H_2 bubbles detected optically during the electrolysis is given by expression (5)

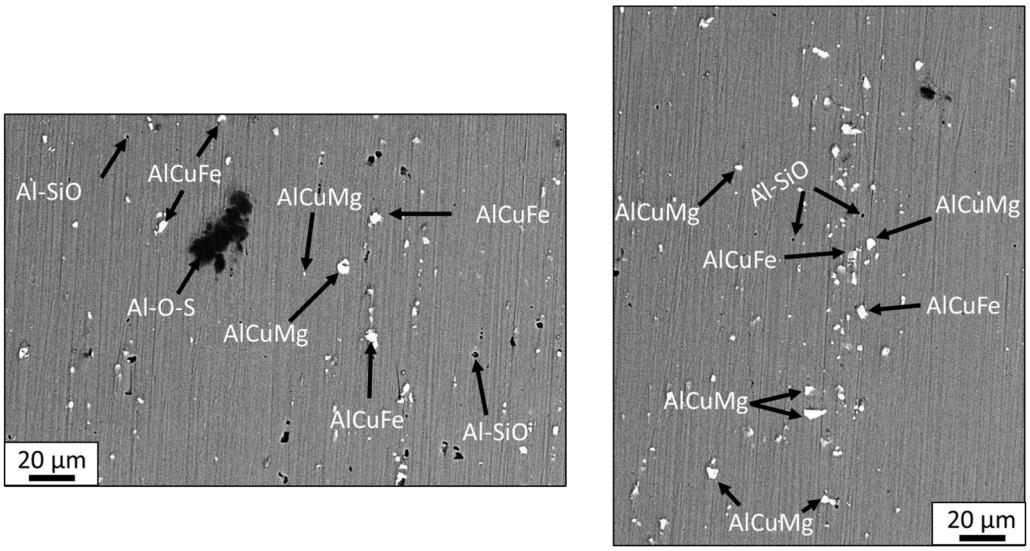

Fig. 13. SEM images (BSE) of the surface after degradation and polishing to the interface.

$$i_{tot} = N \times i_B = N \times \frac{\rho \times V}{M \times t_{H_2}} \times F \times z \quad (5)$$

where N is the number of bubbles counted per image. The evolution of N along the electrolysis is provided in Fig. 9**a**.

Noteworthy, the optically monitored area of the substrate was only a fraction of the surface from which the electrochemical current was measured (around 1 mm^2 out of 50 mm^2). Then, to correlate the total current measured on an unscratched surface and the current related to H_2 bubbles production (calculated from the average H_2 production rate during the experiment), current densities are compared. For this, the bubbles density was estimated. The number of bubbles detected over a 200 μm^2 was counted and by proportionality, a surface area corresponding to the 145 detected bubble generation centers was estimated to be about 1705 μm^2. The current values calculated from Eq. (2) were therefore divided by this surface area, to obtain a normalized current density:

$$j_{tot} = N \times i_B = \frac{N \times \frac{\rho \times V}{M \times t_{H_2}} \times F \times z}{1705\ (\mu m^2)} \quad (6)$$

Evidently, such an evaluation of the electrochemical current density necessary to produce the detected quantity of hydrogen gas can only give an idea of the orders of magnitude, because of the errors in bubble size and bubble lifetime. Assuming two limit values of bubble lifetime defined previously (t_{H2}=0.1 s and t_{H2}=5 s.) and regular bubble production once an active center is formed, two limits of the cathodic current density values were calculated. They are presented in Fig. 7 as the limits of the hachured corridor (black symbols) and compared to the electrochemical current density measured on the unscratched sample (red symbols). Although the corridor is large enough because of the uncertain bubble lifetime on the surface, the orders of magnitude seem to be coherent with the electrochemical measurement. This reveals that the contribution of the IMPs to the reactivity can indeed be considered as the major or at least important process even under 6 µm thick oxide layer. This could later strongly contribute to the destabilization of the oxide because of the localized pH increase at the interface thanks to reaction (1). One could also note that the major difference is observed during the first 300 s of the experiments when no or very small number of bubbles is formed. This seems to be logic because prior to formation of gas bubbles the solution close to the interface needs to be saturated with hydrogen.

Although the results strongly support the importance of buried IMPs for the reactivity of sealed anodized aluminum alloys and suggest that their presence can affect long term stability of the several µm thick oxide, future statistical verifications and methodological improvements seem interesting.

First, the polishing procedure can be optimized to avoid accidental removal of the buried IMPs. For example, a test could be also performed by only removing few microns of the protective layer instead of the whole oxide with an attempt of SEM-EDS with high voltages applied to the thinned oxide layer to try to detect the buried IMPs or with erosion by argon plasma and analysis by time-of-flight secondary ions mass spectrometry (ToF SIMS). Second, more statistics on the nature of the IMPs and verification of possible correlations between the nature and size of IMPs with the frequency of cathodic sites formation could be also interesting to understand the mechanism of the reactivity initiation.

Third, additional potential activation mechanisms still need to be verified. Among them, the role of local inhomogeneities of the top surface (chemical - by initial µm size defect in the sealed layer, or morphological - from roughness or porosity variation) can influence the surface energy and hence modify both water penetration and bubble stability on the surface. SEM-EDS and X-ray photoelectron spectroscopy (XPS) analysis of the considered samples did not reveal major inhomogeneities of the chemical composition on the surface as illustrated in SI, Fig. A3, however, more detailed 3D resolved analysis could be interesting, taking into account the thickness of the layer.

Advanced image analysis of the surface morphology/porosities and advanced chemical analysis of the oxide layer with high spatial resolution should be able to provide additional information to confirm if other important mechanisms are not yet considered or the role of buried IMPs is primordial for stability of anodized and sealed aluminum alloys.

4. Conclusion

This study focused on the development of a new methodology able to detect the initial steps of reactivity of aluminum alloys under a 6 µm thick protective oxide layer and the attempt to correlate them with the presence of buried intermetallic particles in the alloy close to the alloy /oxide interface. The results showed that the sites of nucleating H_2 bubbles can be identified by optical microscopy, through post-experiment optical image treatment, allowing to use the detected H_2 bubbles as a probe of local cathodic reactivity. It was then possible to remove the protective oxide layer and analyze the aluminum alloy close to the interface by SEM-EDS in order to identify and localize the buried IMPs. A statistical comparison of the *in situ* reactivity from the *in situ* RM with the SEM images of the interface buried under this location has

shown that underneath of the most bubbles generation centers a buried IMP was found at the alloy /oxide interface with a distance between the centers of the bubble projection to the interface and the center of the IMP less than the bubble diameter. Taking into account that buried IMPs are not always detected exactly below the bubble, other mechanisms, probably related to local roughness and porosity of the oxide layer are possible. However, the cathodic current density, roughly estimated from the hydrogen bubbles dynamic production, seems to be consistent with the electrochemical current density measured on the intact surface in identical conditions, supporting the importance of the reactivity initiation on IMPs buried under 6 μm thick oxide.

Even if the statistical approach can be improved, several important conclusions could be drawn from this work:

1) Coupling accelerated degradation procedure with high resolution *in situ* reflective microscopy and *ex-situ* SEM-EDS analysis of the substrate allows to detect initial reactivity sites and verify their correlation with the substrate microstructure.
2) 80% of the sites of cathodic reactivity on TSA anodized AA7175 are located in the areas of the oxide, under which buried intermetallic particles in the substrate were detected.
3) Correlation between the position of buried IMPs and sites of initial cathodic reactivity confirms the proposed in [28] degradation mechanism of silicate sealed anodized layer, in which buried IMPs act as local cathodes resulting in local pH increase and dissolution of the oxide close to the buried alloy/oxide interface and surrounding metallic matrix.

Naturally, these conclusions apply only for the studied sealed system. However, they alert that for other systems, similar effects could occur and should not be neglected.

CRediT authorship contribution statement

Florian Raffin: Writing – review & editing, Writing – original draft, Visualization, Validation, Investigation, Formal analysis, Data curation. **Aleksei Makogon:** Writing – original draft, Visualization, Validation, Software, Investigation, Formal analysis, Data curation. **Frédéric Kanoufi:** Writing – review & editing, Validation, Supervision, Methodology. **Jacques Echouard:** Writing – review & editing, Validation, Resources. **Viacheslav Shkirskiy:** Writing – review & editing, Validation, Supervision, Methodology, Investigation, Formal analysis, Conceptualization. **Polina Volovitch:** Writing – review & editing, Writing – original draft, Validation, Supervision, Methodology, Formal analysis, Conceptualization.

Declaration of competing interest

The authors declare that they have no known competing financial interests or personal relationships that could have appeared to influence the work reported in this paper.

Data availability

Data will be made available on request.

Supplementary materials

Supplementary material associated with this article can be found, in the online version, at doi:10.1016/j.electacta.2024.144155.

References

[1] C. Vargel. Corrosion of Aluminium, 2nd ed., Elsevier, 2020 https://doi.org/10.1016/C2012-0-02741-X.
[2] J.R. Davis, (Ed.), Corrosion of Aluminum and Aluminum Alloys, ASM International, ISBN 978-0-87170-629-4, 1999.
[3] D. Mata, M. Serdechnova, M. Mohedano, C.L. Mendis, S.V. Lamaka, J. Tedim, T. Hack, S. Nixon, M.L. Zheludkevich, Hierarchically organized Li–Al-LDH nanoflakes: a low-temperature approach to seal porous anodic oxide on aluminum alloys, RSC Adv. 7 (2017) 35357–35367, https://doi.org/10.1039/C7RA05593E.
[4] T. Sanchez, S. Gillet, V. Shkirskiy, V. Vivier, J. Echouard, J. Światowska, P. Volovitch, New experimental approach for intelligent screening of buried metal/oxide/polymer interfaces via local electrochemistry: example of undamaged model epoxy-coated Zn alloys, Electrochim. Acta 367 (2021) 137411, https://doi.org/10.1016/j.electacta.2020.137411.
[5] F. Mansfeld, M.W. Kendig, Electrochemical impedance spectroscopy of protective coatings, Mater. Corros. 36 (1985) 473–483, https://doi.org/10.1002/maco.19850361102.
[6] M.G. Olivier, M. Poelman, Use of electrochemical impedance spectroscopy (EIS) for the evaluation of electrocoatings performances, in: R. Shoja Razavi (Ed.). Recent Researches in Corrosion Evaluation and Protection, InTech, 2012, https://doi.org/10.5772/33844.
[7] F. Meng, L. Liu, Electrochemical evaluation technologies of organic coatings, in: J. Andres Perez-Taborda, A. G. Avila Bernal (Eds.). Coatings and Thin-Film Technologies, IntechOpen, 2019, https://doi.org/10.5772/intechopen.79736.
[8] J.J. Suay, E. Giménez, T. Rodríguez, K. Habbib, J.J. Saura, Characterization of anodized and sealed aluminium by EIS, Corros. Sci. 45 (2003) 611–624, https://doi.org/10.1016/S0010-938X(02)00137-3.
[9] T. Sanchez, E. Kurchavova, V. Shkirskiy, J. Światowska, V. Vivier, P. Volovitch, Detection and quantification of defect evolution at buried metal-oxide-polymer interface on rough substrate by local electrochemical impedance mapping, Electrochim. Acta 388 (2021) 138467, https://doi.org/10.1016/j.electacta.2021.138467.
[10] V. Shkirskiy, P. Volovitch, V. Vivier, Development of quantitative local electrochemical impedance mapping: an efficient tool for the evaluation of delamination kinetics, Electrochim. Acta 235 (2017) 442–452, https://doi.org/10.1016/j.electacta.2017.03.076.
[11] F. Zou, A high-resolution probe for localized electrochemical impedance spectroscopy measurements, J. Electrochem. Soc. 144 (1997) 8, https://doi.org/10.1149/1.1837729.
[12] F. Zou, D. Thierry, Localized electrochemical impedance spectroscopy for studying the degradation of organic coatings, Electrochim. Acta 42 (1997) 3293–3301, https://doi.org/10.1016/S0013-4686(97)00180-1.
[13] V. Upadhyay, D. Battocchi, Localized electrochemical characterization of organic coatings: a brief review, Prog. Org. Coat. 99 (2016) 365–377, https://doi.org/10.1016/j.porgcoat.2016.06.012.
[14] A.C. Bastos, O.V. Karavai, M.L. Zheludkevich, K.A. Yasakau, M.G.S. Ferreira, Localised measurements of pH and dissolved oxygen as complements to SVET in the investigation of corrosion at defects in coated aluminum alloy, Electroanalysis. 22 (2010) 8, https://doi.org/10.1002/elan.201000076.
[15] E. Daviddi, V. Shkirskiy, P.M. Kirkman, M.P. Robin, C.L. Bentley, P.R. Unwin, Nanoscale electrochemistry in a copper/aqueous/oil three-phase system: surface structure–activity-corrosion potential relationships, Chem. Sci. 12 (2021) 3055–3069, https://doi.org/10.1039/D0SC06516A.
[16] L. Grandy, J. Mauzeroll, Localising the electrochemistry of corrosion fatigue, Curr. Opin. Colloid Interface Sci. 61 (2022) 101628, https://doi.org/10.1016/j.cocis.2022.101628.
[17] P.J. Denissen, A.M. Homborg, S.J. Garcia, Interpreting electrochemical noise and monitoring local corrosion by means of highly resolved spatiotemporal real-time optics, J. Electrochem. Soc. 166 (2019) C3275–C3283, https://doi.org/10.1149/2.0341911jes.
[18] V. Shkirskiy, F. Kanoufi, Reflective microscopy for mechanistic insights in corrosion research, Curr. Opin. Electrochem. 39 (2023) 101259, https://doi.org/10.1016/j.coelec.2023.101259.
[19] W. Linpé, G.S. Harlow, A. Larsson, G. Abbondanza, L. Rämisch, S. Pfaff, J. Zetterberg, J. Evertsson, E. Lundgren, An electrochemical cell for 2-dimensional surface optical reflectance during anodization and cyclic voltammetry, Rev. Sci. Instrum. 91 (2020) 044101, https://doi.org/10.1063/1.5133905.
[20] L. Godeffroy, A. Makogon, S. Gam Derouich, F. Kanoufi, V. Shkirskiy, Imaging and quantifying the chemical communication between single particles in metal alloys, Anal. Chem. 95 (2023) 9999–10007, https://doi.org/10.1021/acs.analchem.3c01258.
[21] M. Olgiati, P.J. Denissen, S.J. Garcia, When all intermetallics dealloy in AA2024-T3: quantifying early stage intermetallic corrosion kinetics under immersion, Corros. Sci. 192 (2021) 109836, https://doi.org/10.1016/j.corsci.2021.109836.
[22] P.J. Denissen, V. Shkirskiy, P. Volovitch, S.J. Garcia, Corrosion inhibition at scribed locations in coated AA2024-T3 by cerium- and DMTD-loaded natural silica microparticles under continuous immersion and wet/dry cyclic exposure, ACS Appl. Mater. Interfaces 12 (2020) 23417–23431, https://doi.org/10.1021/acsami.0c03368.
[23] G.E. Totten, D.S. MacKenzie, Handbook of Aluminum. Physical Metallurgy and Processes 1, CRC Press, 2003.
[24] J.S. Safrany, Anodisation de l'aluminium et de ses alliages, Tech. Ing. (2019) 30, https://doi.org/10.51257/a-v4-m1630.
[25] Z. Feng, Y. Liu, T. Hashimoto, G.E. Thompson, X. Zhou, P. Skeldon, Influence of surface pretreatments on the corrosion protection of sol-gel coated AA2024-T3 aluminium alloy: influence of surface pretreatments on the corrosion protection, Surf. Interface Anal. 45 (2013) 1452–1456, https://doi.org/10.1002/sia.5216.

[26] I. Pires, L. Quintino, C.M. Rangel, G.E. Thompson, P. Sheldon, X. Zhou, Influence of pre-treatments on the surface condition of 2024-T3 aluminium alloy, Trans. IMF 78 (2000) 179–185, https://doi.org/10.1080/00202967.2000.11871334.
[27] C.M. Rangel, T.I. Paiva, P.P. da Luz, Conversion coating growth on 2024-T3 Al alloy. The effect of pre-treatments, Surf. Coat. Technol. 202 (2008) 3396–3402, https://doi.org/10.1016/j.surfcoat.2007.12.017.
[28] F. Raffin, M. Magnan, A. Seyeux, S. Zanna, J. Echouard, J. Swiatowska, P. Volovitch, Intermetallic particles distribution in 7XXX series aluminium alloy substrate impacts cathodic stability of silicate sealed anodized oxide, Corros. Sci. (submitted 04/01/2024).
[29] H. Leidheiser, Cathodic delamination of polybutadiene from steel-A review, J. Adhes. Sci. Technol. 1 (1987) 79–98, https://doi.org/10.1163/156856187X00094.
[30] A.J. Bard, L.R. Faulkner. Electrochemical methods fundamentals and applications. pdf, 2nd ed., 2000, p. 864.
[31] B.J. Usman, F. Scenini, M. Curioni, Exploring the use of an AC-DC-AC technique for the accelerated evaluation of anticorrosion performance of anodic films on aluminium alloys, Prog. Org. Coat. 144 (2020) 105648, https://doi.org/10.1016/j.porgcoat.2020.105648.
[32] N. Sukiman, X. Zhou, N. Birbilis, A.E. Hughes, J.M.C. Mol, S. J, X. Zhou, G. E, Durability and corrosion of aluminium and its alloys: overview, property space, techniques and developments, in: Z. Ahmad (Ed.). Aluminium Alloys–New Trends in Fabrication and Applications, InTechOpen, 2012, p. 52, https://doi.org/10.5772/53752.
[33] R. Saillard, B. Viguier, G. Odemer, A. Pugliara, B. Fori, C. Blanc, Influence of the microstructure on the corrosion behaviour of 2024 aluminium alloy coated with a trivalent chromium conversion layer, Corros. Sci. 142 (2018) 119–132, https://doi.org/10.1016/j.corsci.2018.07.007.
[34] L. Hao, B.R. Cheng, Sealing processes of anodic coatings–past, present, and future, Met. Finish. 98 (2000) 11, https://doi.org/10.1016/S0026-0576(01)80002-7.
[35] B. Rachel Cheng, L. Hao, Comparative study of the effects of sealing processes on the wear resistance and the sealing quality of hard anodic coatings, Met. Finish. 98 (2000) 48–55, https://doi.org/10.1016/S0026-0576(00)81731-6.
[36] V. Cartigny, D. Veys-Renaux, P. Desenne, E. Rocca, Rapid sealing of an alumina nanoporous network grown by anodizing and dye-filled, Surf. Coat. Technol. 364 (2019) 369–376, https://doi.org/10.1016/j.surfcoat.2019.03.004.
[37] R. Gaggiano, P. Moriamé, M. Biesemans, I. De Graeve, H. Terryn, Mechanism of formation of silicate thin films on porous anodic alumina, Surf. Coat. Technol. 205 (2011) 5210–5217, https://doi.org/10.1016/j.surfcoat.2011.05.029.
[38] M. Malki, V. Abbas, Controlling aluminium silicate formation in membrane separation processes, in: Proceedings of the International Desalination Association World Congress on Desalination and Water Reuse, 2013. IDAWC/TIAN13-252.
[39] H. Isaacs, A. Haughton, A. Shipley, H. Popenoe, E. Plus, J. Lumsden, Direct image processing of corroding surfaces applied to friction stir welding, Proc. Electrochem. Soc. 23 (2003).
[40] J.F. Lemineur, P. Ciocci, J.M. Noël, H. Ge, C. Combellas, F. Kanoufi, Imaging and quantifying the formation of single nanobubbles at single platinum nanoparticles during the hydrogen evolution reaction, ACS Nano 15 (2021) 2643–2653, https://doi.org/10.1021/acsnano.0c07674.
[41] N. Birbilis, R.G. Buchheit, Electrochemical characteristics of intermetallic phases in aluminum alloys, J. Electrochem. Soc. 152 (2005) B140, https://doi.org/10.1149/1.1869984.
[42] N. Birbilis, R.G. Buchheit, Investigation and discussion of characteristics for intermetallic phases common to aluminum alloys as a function of solution pH, J. Electrochem. Soc. 155 (2008) C117, https://doi.org/10.1149/1.2829897.
[43] P. Volovitch, J.E. Masse, A. Fabre, L. Barrallier, W. Saikaly, Microstructure and corrosion resistance of magnesium alloy ZE41 with laser surface cladding by Al–Si powder, Surf. Coat. Technol. 202 (2008) 4901–4914, https://doi.org/10.1016/j.surfcoat.2008.04.052.
[44] M. Saenz de Miera, M. Curioni, P. Skeldon, G.E. Thompson, Preferential anodic oxidation of second-phase constituents during anodising of AA2024-T3 and AA7075-T6 alloys, Surf. Interface Anal. 42 (2010) 241–246, https://doi.org/10.1002/sia.3191.
[45] A. Renaud, M. Poorteman, J. Escobar, L. Dumas, Y. Paint, L. Bonnaud, P. Dubois, M.G. Olivier, A new corrosion protection approach for aeronautical applications combining a Phenol-paraPhenyleneDiAmine benzoxazine resin applied on sulfo-tartaric anodized aluminum, Prog. Org. Coat. 112 (2017) 9, https://doi.org/10.1016/j.porgcoat.2017.07.007.
[46] F. Snogan, C. Blanc, G. Mankowski, N. Pébère, Characterisation of sealed anodic films on 7050 T74 and 2214 T6 aluminium alloys, Surf. Coat. Technol. 154 (2002) 94–103, https://doi.org/10.1016/S0257-8972(01)01717-0.
[47] M. Curioni, M. Saenz de Miera, P. Skeldon, G.E. Thompson, J. Ferguson, Macroscopic and local filming behavior of AA2024 T3 aluminum alloy during anodizing in sulfuric acid electrolyte, J. Electrochem. Soc. 155 (2008) C387, https://doi.org/10.1149/1.2931522.
[48] K. Giffard, Etude Mécanismes Colmatage Films Anodiques Alliage D'alu 2024, Thèse de Doctorat,Université de Toulouse, 2015, 180 p. (in french), http://theses.ups-tlse.fr/3010/1/2015TOU30319.pdf.
[49] S. Lebouil, J. Tardelli, E. Rocca, P. Volovitch, K. Ogle, Dealloying of Al2Cu, Al7Cu2Fe, and Al2CuMg intermetallic phases to form nanoparticulate copper films, Mater. Corros. 65 (2014) 416–424, https://doi.org/10.1002/maco.201307550.
[50] Lifetime of surface bubbles, Laboratoire NAVIER (n.d.). https://navier-lab.fr/lifetime-of-liquid-films/(accessed April 26, 2023).